


 Cite this: *RSC Adv.*, 2020, 10, 6927

3D-QSAR, molecular docking, and molecular dynamics simulation study of thieno[3,2-*b*]pyrrole-5-carboxamide derivatives as LSD1 inhibitors†

 Yongtao Xu,^{id}*^{abc} Zihao He,^{abc} Hongyi Liu,^{abc} Yifan Chen,^{abc} Yunlong Gao,^{abc} Songjie Zhang,^{abc} Meiting Wang,^{abc} Xiaoyuan Lu,^a Chang Wang,^a Zongya Zhao,^a Yan Liu,^a Junqiang Zhao,^a Yi Yu^a and Min Yang^{*abc}

Histone Lysine Specific Demethylase 1 (LSD1) is overexpressed in many cancers and becomes a new target for anticancer drugs. In recent years, small molecule inhibitors with various structures targeting LSD1 have been reported. Here we report the binding interaction modes of a series of thieno[3,2-*b*]pyrrole-5-carboxamide LSD1 inhibitors using molecular docking, and three-dimensional quantitative structure–activity relationships (3D-QSAR). Comparative molecular field analysis (CoMFA $q^2 = 0.783$, $r^2 = 0.944$, $r_{\text{pred}}^2 = 0.851$) and comparative molecular similarity indices analysis (CoMSIA $q^2 = 0.728$, $r^2 = 0.982$, $r_{\text{pred}}^2 = 0.814$) were used to establish 3D-QSAR models, which had good verification and prediction capabilities. Based on the contour maps and the information of molecular docking, 8 novel small molecules were designed *in silico*, among which compounds **D4**, **D5** and **D8** with high predictive activity were subjected to further molecular dynamics simulations (MD), and their possible binding modes were explored. It was found that Asn535 plays a crucial role in stabilizing the inhibitors. Furthermore, ADME and bioavailability prediction for **D4**, **D5** and **D8** were carried out. The results would provide valuable guidance for designing new reversible LSD1 inhibitors in the future.

 Received 2nd December 2019
 Accepted 1st February 2020

DOI: 10.1039/c9ra10085g

rsc.li/rsc-advances

Introduction

Histone modification is an important epigenetic modification including acetylation, methylation and phosphorylation.¹ Gene expression is regulated by controlling the conformational transformation of chromosomes between heterochromatin with transcriptional inhibition and euchromatin with transcriptional activation.² Histone methylation was considered to be an irreversible process until the discovery of LSD1 (also known as KDM1A) in 2004, revealing that histone methylation was a dynamically reversible process.³ LSD1 is a highly conserved flavin adenine dinucleotide (FAD) dependent amine oxidase that can specifically remove the single-dimethylation of histone lysine H3K4 and H3K9.⁴ LSD1 can also remove the methyl of many proteins, such as p53, DNA methyltransferase 1 (DNMT1), signal transducer and activator of transcription 3 (STAT3), E2F transcription factor 1 and so on, thereby regulating the

physiological functions of downstream cell.^{5–9} Studies have shown that LSD1 is highly expressed in a variety of tumor cells, for example breast cancer, neuroblastoma, lung cancer, gastric cancer, acute myeloid leukemia and so on.^{10–14} It has been shown in many animal experiments that the use of small-molecule inhibitors to inhibit the expression of LSD1 can effectively inhibit the differentiation, proliferation, invasion and metastasis of cancer cells, as well as the growth of tumors.^{15–17} These studies indicated that LSD1 not only had important biological significance, but also provided a new method for cancer treatment with LSD1 small molecule inhibitors.

The research on LSD1 inhibitors has attracted increasing interest since the discovery of LSD1. As a member of the monoamine oxidase (MAO) family, LSD1 has high sequences similarity with homologous protein MAOs, so MAO inhibitors can be used to inhibit the activity of LSD1.¹⁸ MAO inhibitors such as tranlycypromine (TCPA, Fig. 1A), pargyline (Fig. 1B), phenelzine (Fig. 1C) have low inhibitory activity and poor selectivity for LSD1, but a series of high activity and high selective inhibitors have been optimized or designed based on them.¹⁹ Among the TCPA-based series inhibitors, ORY-1001 (Fig. 1D) entered phase II clinical trials about acute myelogenous leukemia (AML) in 2013. GSK2879552 (Fig. 1E) also entered I period clinical used in the treatment of relapsed or refractory small cell lung cancer (SCLC).^{20,21} In addition to these

*School of Biomedical Engineering, Xinxiang Medical University, Xinxiang, Henan, 453003, China. E-mail: yxu@xxmu.edu.cn; yangmin@xxmu.edu.cn

^bXinxiang Key Laboratory of Biomedical Information Research, Xinxiang, Henan, 453003, China

^cHenan Engineering Laboratory of Combinatorial Technique for Clinical and Biomedical Big Data, Xinxiang, Henan, 453003, China

† Electronic supplementary information (ESI) available. See DOI: 10.1039/c9ra10085g



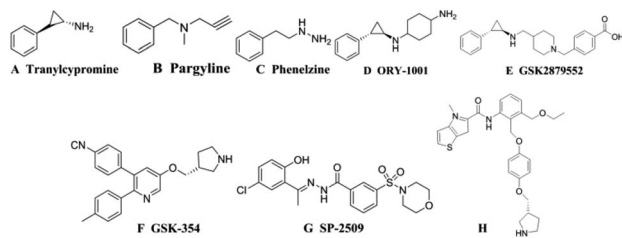


Fig. 1 Structures of several reported LSD1 inhibitors.

irreversible inhibitors covalently bound with FAD, some reversible inhibitors with non-covalently bound were also designed. The IC_{50} of the reversible inhibitor GSK-354 (Fig. 1F) reached 90 nM.²² SP-2509 (Fig. 1G) was highly active and selective, and its IC_{50} value *in vitro* reached 13 nM.²³ In 2017, thieno[3,2-*b*]pyrrolo-5-carboxamides (Fig. 1H) class reversible inhibitors were reported. The highest IC_{50} value of these compounds was 7.8 nM, which displayed a remarkable effect on MLL-AF9 human leukemia cell.^{24,25}

LSD1 has great potential in the research and development of anti-cancer drugs, and the design of LSD1 with high efficiency and selectivity has become the research goal of drug workers. At present, irreversible LSD1 inhibitors have been introduced into clinical trials. However, despite the good LSD1 inhibitory activity they have shown, there are still many defects: potential selectivity to MAO, strong side effects, and difficult synthesis. Reversible inhibitors have strong selectivity and small side effects, but no reversible inhibitors have entered clinical trials. Therefore, the design of highly effective reversible LSD1 inhibitors has become the focus of research in recent years.

In vitro activity determination of small molecule inhibitors is time-consuming and costly. The computer-aided drug design (CADD) can not only preliminarily predict the activity of inhibitors, but also save experimental costs and provide a guidance for designing more effective inhibitors by exploring the reaction mechanism of inhibitors at the molecular level.²⁶ A series of 1,2,4-triazine derivatives as new h-HAAO inhibitors using 3D-QSAR, docking and MD and three of these inhibitors were tested *in silico* associated with relatively high activities.²⁷ The 3D-QSAR method was also used to explain flavonoids inhibitors for *Escherichia coli*, and molecular docking was performed to predict the binding mode.²⁸ Ma *et al.* analyzed pyrazolo[3,4-*d*]pyrimidine derivatives as the TgCDPK1 inhibitors using the 3D-QSAR, docking, dynamics simulation, and then designed some new inhibitors.²⁹ Therefore, the application of CADD methods into the research of LSD1 inhibitors should be efficient for designing new and highly active LSD1 inhibitors.

In this study, 55 small molecules were selected from a series of thieno[3,2-*b*]pyrrolo-5-carboxamide (Fig. 1H) compounds.^{24,25} The crystal structures of five small molecules with LSD1 have been reported, but the binding modes of the remaining 50 small molecules with LSD1 were still uncertain. In order to explain the structure–activity relationship and explore the possible optimization direction for such inhibitors, the 3D-QSAR model was developed based on the docking poses. Contour maps could

provide theoretical guidance for designing new inhibitors. According to the molecular docking results and contour maps, 8 new molecule inhibitors with high predictive activity were designed. The binding modes of 3 new molecule inhibitors with the highest activity were explored by molecular docking and molecular dynamics simulations. The present research would provide valuable guidance for the design of new LSD1 inhibitors.

Materials and methods

Data sets

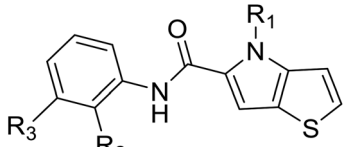
55 compounds that were previously assessed for their LSD1 inhibition activities were used as the data set (Table 1).^{24,25} These compounds share a common thieno[3,2-*b*]pyrrolo-5-carboxamide scaffold and introducing a substituted chiral pyrrolidine group at the R₂ position of the parent scaffold resulted in significantly improved activities, *i.e.* 51, 54 and 55. CoMFA³⁰ and CoMSIA³¹ were used to establish 3D-QSAR models. In these two models, different molecular properties were used as independent variables to calculate the relationship between their structure and biological activities, while pIC_{50} ($-\log IC_{50}$) was also used as the dependent variable. The range of pIC_{50} values was from 4.046 to 8.174 in all data sets. The data set was partitioned randomly with the following criteria: the pIC_{50} values of the compounds in the test set should be distributed in various orders of magnitude in proportion to the whole set. At the same time, the structures of the compounds in the test set should sufficiently represent the diversity of the whole dataset. Finally, 43 compounds (78% of total compounds) were selected as the training set for the construction of CoMFA and CoMSIA models, and the remaining 12 compounds (22% of total compounds) were selected as an independent test set for validating the reliability of the model. The distribution of pIC_{50} values for the whole set, the training set and test set were shown in Fig. S1.† The structures and activity data of all compounds are shown in Table 1.

Molecular docking

Molecular docking and the establishment of CoMFA and CoMSIA models were completed in SYBYL-X2.0 (2.0, Tripos International, St. Louis, MS, USA). The 3D structures of 55 small molecules were obtained in the sketch module. Energy minimization was performed using Powell gradient algorithm with a maximum of 1000 iterations, the convergence criterion was limited to 0.001 kcal mol⁻¹ Å⁻¹. All compounds were calculated by Gasteiger–Huckel charges using the Tripos force field. The top-scored docked poses are not always the most reasonable pose for the specific system. Therefore, we selected the docked poses based on the docking scores as well as empirical criteria Essential Chemical Interactions Described for Analogue Ligands (ECIDALs),³² which is defined from previous literature or crystal structure. The reported crystal structures of LSD1 in complex with 5 ligands (compounds 25, 16, 36, 54 and 55 in Table 1) were obtained from Protein Data Bank (PDB codes: 5LGT, 5LGN, 5LGU, 5LHH and 5LHI). Complex (PDB codes:



Table 1 The structures, the actual and predicted activities by CoMFA & CoMSIA models of LSD1 inhibitors^a



scaffold A

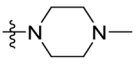
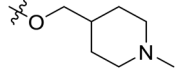
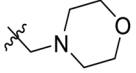
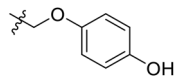
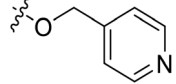
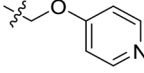
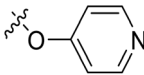
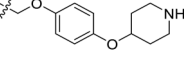
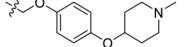
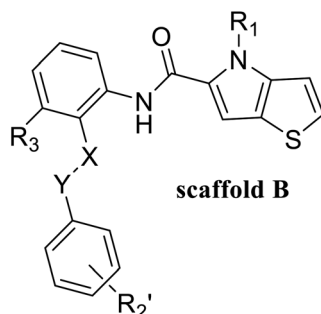
No.	R ₁	R ₂	R ₃	IC ₅₀ (μM)	pIC ₅₀	CoMFA		CoMSIA	
						Pred.	Res.	Pred.	Res.
1*	CH ₃	H	H	25.7	4.590	4.325	0.27	4.518	0.07
4	Et	H	H	9.3	5.032	4.401	0.63	4.607	0.42
5	-CH ₂ CH ₂ NH ₂	H	H	48.1	4.318	4.075	0.24	4.434	-0.12
6*	Pr	H	H	53.2	4.274	4.274	0.00	4.633	-0.36
7	CH ₃	H	-Cl	18.7	4.728	4.545	0.18	4.509	0.22
8	CH ₃	H		21.5	4.668	4.850	-0.18	4.753	-0.08
9	CH ₃	H	-F	22.2	4.654	4.439	0.21	4.526	0.13
10	CH ₃	H	-OCH ₃	26.5	4.577	4.611	-0.03	4.637	-0.06
11	CH ₃	H	-N(Me) ₂	29.6	4.529	4.781	-0.25	4.662	-0.13
12*	CH ₃	H	-CONH ₂	97.3	4.012	4.604	-0.59	4.601	-0.59
13	CH ₃	H		2.2	5.658	5.440	0.22	5.702	-0.04
14	CH ₃	H	-CH ₂ SMe	7.4	5.131	4.892	0.24	4.855	0.28
15*	CH ₃	H		11.1	4.955	4.704	0.25	4.804	0.15
16	CH ₃	H	-CH ₂ OMe	13.4	4.873	4.786	0.09	4.854	0.02
17	CH ₃	H	-CH ₂ N(Me) ₂	16.7	4.777	4.415	0.36	4.748	0.03
18	CH ₃	H		25.2	4.599	4.745	-0.15	4.607	-0.01
19	CH ₃	H	-CH ₂ OH	52.3	4.281	4.701	-0.42	4.569	-0.29
20*	CH ₃	H		7.2	5.143	4.687	0.46	4.258	0.88
21	CH ₃	H		9.4	5.027	4.765	0.26	4.903	0.12
22	CH ₃	H		89.9	4.046	4.605	-0.56	4.252	-0.21
23	CH ₃	H		0.162	6.790	7.090	-0.30	6.735	0.05
24	CH ₃	H		0.442	6.355	6.567	-0.21	6.386	-0.03



Table 1 (Contd.)



No.	X	Y	R ₁	R ₂	R ₃	IC ₅₀ (μM)	pIC ₅₀	CoMFA		CoMSIA		
								Pred.	Res.	Pred.	Res.	
25	C	O	CH ₃		p-	H	0.31	6.509	6.668	-0.16	6.515	-0.01
26*	C	O	CH ₃		p-	H	0.09	7.046	6.523	0.52	6.550	0.50
27*	C	O	CH ₃		m-	H	1	6.000	5.755	0.24	5.481	0.52
28	C	O	CH ₃		o-	H	68.2	4.166	4.048	0.12	4.045	0.12
29	C	C	CH ₃		p-	H	0.177	6.752	6.63	0.12	6.664	0.09
30*	O	C	CH ₃		p-	H	0.336	6.474	6.741	-0.27	6.621	-0.15
31	C	O	CH ₃		p-	H	1.5	5.824	6.304	-0.48	5.817	0.01
33	Carbonyl	NH	CH ₃		p-	H	2.2	5.658	5.947	-0.29	5.631	0.02
34	C	O	CH ₃		p-	H	2.5	5.602	6.162	-0.56	5.563	0.04
35	C	O	CH ₃		p-	H	2.9	5.538	5.812	-0.27	5.487	0.05
36	C	O	CH ₃		p-	H	0.018	7.745	7.192	0.55	7.401	0.34
37	C	O	CH ₃		p-	H	0.064	7.194	6.873	0.32	6.974	0.22
38	C	O	CH ₃		p-	H	0.121	6.917	6.813	0.10	6.987	-0.07

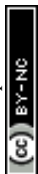
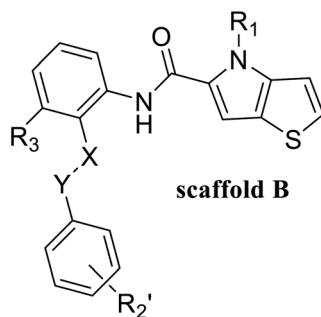


Table 1 (Contd.)



No.	X	Y	R ₁	R' ₂	R ₃	IC ₅₀ (μM)	pIC ₅₀	CoMFA		CoMSIA	
								Pred.	Res.	Pred.	Res.
39	C	O	CH ₃		H	0.149	6.827	6.98	-0.15	7.230	-0.40
40	C	O	CH ₃		H	0.209	6.680	6.378	0.30	6.790	-0.11
41	C	O	CH ₃		H	0.451	6.346	6.156	0.19	6.242	0.10
42	C	O	CH ₃		H	0.618	6.209	6.272	-0.06	6.271	-0.06
43	C	O	CH ₃		H	0.674	6.171	6.523	-0.35	6.262	-0.09
44	C	O	CH ₃		H	0.804	6.095	6.012	0.08	6.290	-0.19
45	C	O	CH ₃		H	1.3	5.886	5.995	-0.11	5.879	0.01
46*	C	O	CH ₃		H	3.2	5.495	4.571	0.92	5.319	0.18
47*	C	O	CH ₃		-COMe	0.075	7.125	6.522	0.60	6.959	0.17
48	C	O	CH ₃		-COEt	0.056	7.252	7.182	0.07	7.313	-0.06
49	C	O	CH ₃			0.065	7.187	7.031	0.16	7.098	0.09
50	C	O	CH ₃		-COiPr	0.066	7.180	7.317	-0.14	7.106	0.07
51*	C	O	CH ₃		-COMe	0.0084	8.076	7.829	0.25	8.290	-0.21

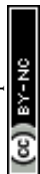
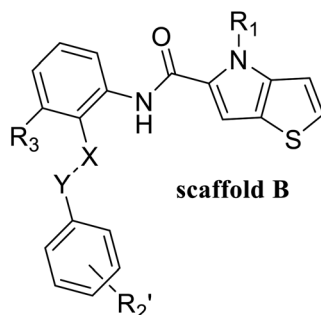
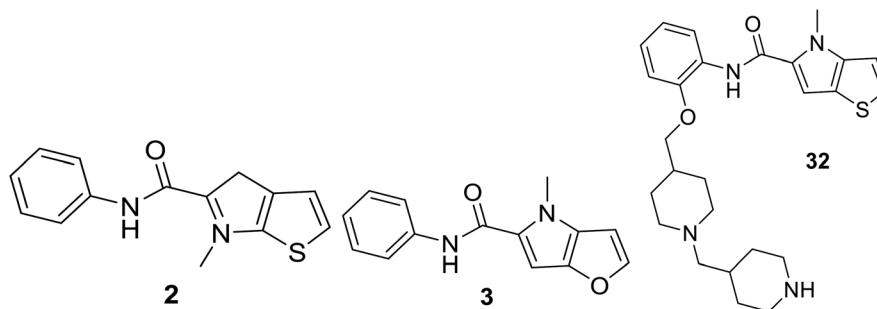


Table 1 (Contd.)



No.	X	Y	R ₁	R ₂ '	R ₃	IC ₅₀ (μM)	pIC ₅₀	CoMFA		CoMSIA	
								Pred.	Res.	Pred.	Res.
52	C	O	CH ₃		-COMe	0.0292	7.535	7.649	-0.11	7.597	-0.06
53	C	O	CH ₃		-COMe	0.0857	7.067	7.14	-0.07	7.07	0.00
54	C	O	Et		-COMe	0.0067	8.174	7.856	0.32	8.175	0.00
55	C	O	Me		-COEt	0.0078	8.108	7.752	0.36	8.148	-0.04



No.	IC ₅₀ (μM)	pIC ₅₀	CoMFA		CoMSIA	
			Pred.	Res.	Pred.	Res.
2	38.8	4.411	4.453	-0.04	4.459	-0.05
3	89.5	4.048	4.269	-0.22	4.369	-0.32
32*	1.7	5.77	5.321	0.45	4.632	1.14

^a Pred. = predicted pIC₅₀; Res. = residual; *o* = *ortho*-, *m* = *meta*-, *p* = *para*-; * compounds in test set.

5LHH) with the highest ligand activity was used for all 55 compounds molecular docking. The docked poses were selected consistent with orientation retrieved from ECIDALs. Crystal water, metal ions and the original ligand were removed and hydrogen atoms were added before molecular docking. Each small molecule produced 20 docking poses, and the optimal

pose was selected for further study by combining ECIDALs and docking scores.

Molecular alignment

The quality of molecular alignment was considered as a key factor for the robustness and predictive power of CoMFA and



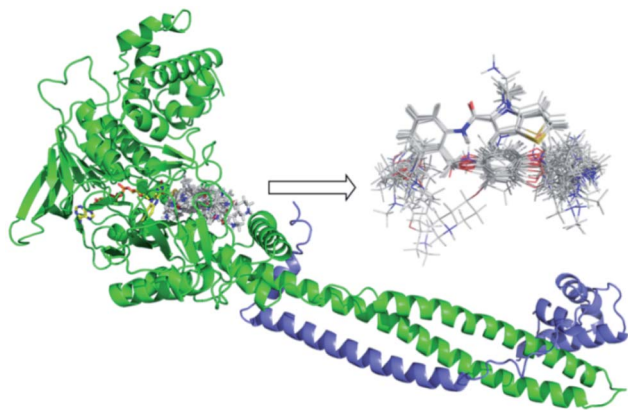


Fig. 2 Docking results of small molecules in the active pocket and the alignment based on docking conformation for all ligands. FAD was shown in yellow and Corest was shown in blue.

CoMSIA models.³³ There are three major approaches to alignment based on common skeletal alignment, pharmacophore alignment and molecular docking alignment, respectively. Both of the former two methods could not reflect the ligand–receptor binding mode correctly. So we chose molecular docking alignment to build 3D-QSAR Models, the optimal docking poses of each small molecule were saved and used in the establishment of the QSAR model. The alignment result of all molecules docking-based pose was shown in Fig. 2.

The alignment results of 43 training set compounds based on docking conformation are shown in Fig. S2.†

3D-QSAR studies

In CoMFA analysis, the steric field and electrostatic field were calculated by Lennard Jones and coulombic potential functions respectively. In the calculation process, the compound was placed in the spatial grids, which consists of many grids with a side length of 2 Å. In this space sp^3 hybridised carbon atom is used as probe particle to calculate the structural characteristics of compound. The van der Waals radius of the probe particle was 1.52 Å and the net charge was +1.0. The energy cut-off value was set to 30 kcal mol⁻¹ and the default value was adopted for other parameters.³⁴ For CoMSIA, in addition to calculating the steric field and electrostatic field parameters, hydrophobic field, hydrogen bond acceptor field and hydrogen bond donor field parameters were also calculated. Therefore, for the probe particle, in addition to the van der Waals radius of 1.52 Å and the net charge of +1.0, while hydrophobic parameters, hydrogen bond acceptor parameters and hydrogen bond donor parameters also should be set to +1 for calculating the compound characteristics.³⁵ The attenuation coefficient was set to 0.3 in default. In the CoMSIA model, Gaussian functions were used to determine the distance between molecule atoms and probe atoms.³⁶

The partial least square (PLS) method was used to analyze CoMFA and CoMSIA models. Cross-validation analysis was carried out with leave-one-out (LOO) to obtain the cross-validation coefficient q^2 and the optimal number of

components (ONC).³⁷ The cross-validation coefficient q^2 could be get as follows:³⁸

$$q^2 = 1 - \frac{\text{PRESS}}{\text{PRESS}_0} \quad (1)$$

In the formula, PRESS represents the sum of the squares of the difference between the predicted and the actual pIC_{50} values and PRESS_0 is the actual pIC_{50} value. The non-cross-validated correlation coefficient (r^2), F -statistic values (F), standard error of estimate (SEE) and contributions of each field were calculated.³⁹ The predictive correlation coefficient (r_{pred}^2) value could be obtained to measure the predictive capability of the 3D-QSAR models. It can be obtained by the formula:⁴⁰

$$r_{\text{pred}}^2 = 1 - \frac{\text{PRESS}}{\text{SD}} \quad (2)$$

In the formula, SD is the sum of the squared deviations between the pIC_{50} values in the test set and mean pIC_{50} in training set; PRESS stands for the sum of squared deviations between predicted pIC_{50} values and actual pIC_{50} values in the test set.

In order to further evaluate the true predictive abilities, external validation parameters R^2 , k , k' , R_0^2 , $R_0'^2$, r_m^2 need to be calculated. R^2 is the correlation coefficient between the observed and predicted activities in the test set with the (0, 0) intercept. R_0^2 and k are the correlation coefficient between the experimental (x) versus predicted activities (y) for the test set through origin and the corresponding slope of regression line. $R_0'^2$ and k' are the correlation coefficients between the predicted (y) versus experimental activities (x) for the test set through origin and the corresponding slope of regression line. The calculation formulas are as follows:⁴¹

$$R^2 = \frac{[\sum(Y_{\text{obs}} - \overline{Y_{\text{obs}}})(Y_{\text{pred}} - \overline{Y_{\text{pred}}})]^2}{\sum(Y_{\text{pred}} - \overline{Y_{\text{pred}}})^2 \times \sum(Y_{\text{obs}} - \overline{Y_{\text{obs}}})^2} \quad (3)$$

$$k = \frac{\sum(Y_{\text{obs}} \times Y_{\text{pred}})}{\sum(Y_{\text{pred}})^2} \quad (4)$$

$$k' = \frac{\sum(Y_{\text{obs}} \times Y_{\text{pred}})}{\sum(Y_{\text{obs}})^2} \quad (5)$$

$$R_0^2 = 1 - \frac{\sum(Y_{\text{obs}} - k \times Y_{\text{pred}})^2}{\sum(Y_{\text{obs}} - \overline{Y_{\text{obs}}})^2} \quad (6)$$

$$R_0'^2 = 1 - \frac{\sum(Y_{\text{pred}} - k' \times Y_{\text{obs}})^2}{\sum(Y_{\text{pred}} - \overline{Y_{\text{pred}}})^2} \quad (7)$$

$$r_m^2 = R^2 \times \left(1 - \sqrt{R^2 - R_0^2}\right) \quad (8)$$

Among them, Y_{obs} and Y_{pred} represent the experimental and predicted activities in the test set, $\overline{Y_{\text{obs}}}$ and $\overline{Y_{\text{pred}}}$ are the average value of the experimental or predicted activities in the test set.



The model is acceptable if the parameters in the 3D-QSAR model meet the following criteria:⁴²

$$q^2 > 0.5$$

$$r_{\text{pred}}^2 > 0.6$$

$$\frac{(R^2 - R_0^2)}{R^2} < 0.1 \text{ or } \frac{(R'^2 - R_0'^2)}{R'^2} < 0.1$$

$$0.85 \leq k \leq 1.15 \text{ or } 0.85 \leq k' \leq 1.15$$

$$|R_0^2 - R_0'^2| < 0.3$$

$$r_m^2 > 0.5$$

Y-randomization test is usually used to evaluate the robustness of the model.⁴³ The dependent variable y is randomly shuffled while the independent variable x matrix is kept unaltered. The process is repeated many times and for each run, a set of new q^2 and r^2 is generated. If the q^2 and r^2 of the models are low, it indicates the good calibration result is not due to chance correlation and the QSAR model is robust.

Molecular dynamics simulations

In order to prove the reliability of the docking results, the binding mode between the series of compounds and LSD1 protein need to be further investigated, and molecular dynamics simulation was carried out using AMBER14 software package. Using the docking results of ligands with LSD1 as the initial conformation, the parameter file of ligands was generated by Antechamber module. Amberff10 force field was used for receptor protein and GAFF force field was used for ligand molecules.⁴⁴ The water box adopted TIP3P water model with a margin distance of 8 Å. After energy minimization, the complex was heated from 0 K to 300 K during 250 ps in NVT ensemble, the constant pressure of 1 atm was equilibrated at 300 K for another 50 ps. Finally, for compound 54 and newly designed compounds with high predictive activity, 50 ns MD was performed under NPT ensemble with the pressure of 1 atm and 300 K. 5000 frames were extracted the average conformation of MD equilibrium phase (the last 5 ns) for analysis as the result of MD.

Binding free energy calculations

MM/GBSA method was used to calculate binding free energy. 200 snapshots were received from the last 2 ns trajectory file for calculation. The binding free energy formula for protein and ligand were as follows:²⁷

$$\Delta G_{\text{bind}} = \Delta G_{\text{complex}} - \Delta G_{\text{protein}} - \Delta G_{\text{ligand}} = \Delta E_{\text{MM}} + \Delta G_{\text{sol}} - T\Delta S = \Delta E_{\text{vdW}} + \Delta E_{\text{ele}} + \Delta G_{\text{GB}} + \Delta G_{\text{SA}} - T\Delta S$$

In the formula, $\Delta G_{\text{complex}}$ represents the total free energy of protein–ligand complex, $\Delta G_{\text{protein}}$ is the total binding energy of protein in solvents and ΔG_{ligand} means the total binding energy of ligand in solvents. ΔE_{MM} is the interaction energy of protein and ligand under gas-phase, and the energy could be obtained by calculating van der Waals energy ΔE_{vdW} and electrostatic energy ΔE_{ele} . ΔG_{sol} stands for the free energy of solvation, which could be achieved by computing polar solvation energy ΔG_{GB} and non-polar solvation energy ΔG_{SA} . $T\Delta S$ stands for entropy contribution, which is generally ignored, because it consumes a large amount of computing resources and has a weak impact on the results. After calculating the binding free energy, we decomposed the energy onto each residue to obtain the key amino acids which have a great impact on it.

Prediction of ADME and bioavailability

Nowadays, the speed of drug research and development is accelerating, and the number of candidate compounds is increasing. It would waste a lot of resources to put them into experiments directly. Therefore, it is necessary to use computational modeling methods to evaluate their bioavailability and pharmacokinetics. SwissADME web tool (<http://www.swissadme.ch>) was used to predict our new LSD1 inhibitors.⁴⁵

Bioavailability evaluation includes the following aspects: lipophilicity, molecular weight, polarity, saturation. The absorption, distribution, metabolism and excretion (ADME) evaluation includes: human gastrointestinal absorption (HIA), blood–brain barrier (BBB) permeation, cytochrome P450-3A4 (CYP3A4) enzyme inhibition and skin permeation ($\log K_p$). Finally, drug-likeness evaluation of our new compounds was conducted according to Lipinski's rule.⁴⁶

Results and discussion

Validation of docking reliability

Both 3D-QSAR modeling and MD were based on the results of molecular docking, so it was necessary to verify the reliability of docking results: the structures of five compounds 16, 25, 36, 54 and 55 from the docking results, and the crystal structures of those compounds were received from protein data bank (PDB code: 5LGN, 5LGT, 5LGU, 5LHH and 5LHI, respectively). The docking pose of five compounds and their corresponding crystal poses were superimposed, and it can be seen that the crystal pose and the docked pose were almost in the same position, having similar spatial orientations (Fig. S3†), with the RMSDs being 0.78 Å, 1.13 Å, 0.62 Å, 0.69 Å and 1.07 Å, respectively. The result suggested that the docking result was reasonable and could be used for further simulation and analysis. The docked posed were selected by the criteria of ECIDALS. The 5 crystal structures were superposed, and it was found that thieno[3,2-*b*]pyrrol-5-carboxamide structures almost



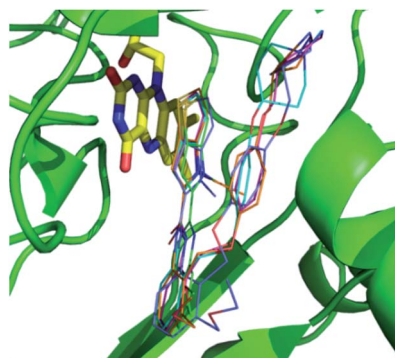


Fig. 3 Superimposing of the ligands from 5 LSD1 crystal structures (PDB: 5LGT (cyan), 5LGN (green), 5LGU (violet), 5LHH (orange) and 5LHI (blue)). FAD is represented by yellow stick, small molecules by line, and protein by green cartoon.

overlapped in the same position (Fig. 3), those features were defined as the ECIDALS of the small molecules that share similar scaffold.

Statistical results of CoMFA and CoMSIA

The stepwise development of CoMFA and possible CoMSIA models using different fields were presented in Table 2.⁴⁷ The internal prediction ability (q^2) and the external prediction ability (r_{pred}^2) were important criteria for measuring the QSAR mode.⁴⁰ CoMFA-S and CoMFA-E were separately modeled using steric field and electrostatic field, and their q^2 values were acceptable, the r_{pred}^2 of CoMFA-S was also acceptable, but the $r_{\text{pred}}^2 < 0.6$ in CoMFA-E indicated that the external prediction ability of the model did not up to the standard. When combined to CoMFA-SE, both q^2 and r_{pred}^2 improved. The result of CoMFA-SE model gave a cross-validated q^2 of 0.783 with an ONC value of 4, a non-cross-validated r^2 of 0.944, a predictive correlation coefficient r_{pred}^2 of 0.851, a SEE value of 0.3, and an F value of 160.128. The contribution of the steric field was 39.4% and 60.6% belonged to electrostatic field.

The CoMSIA-SEHA and CoMSIA-ALL models generated similar q^2 (0.727 and 0.728, respectively). However, the r_{pred}^2 of CoMSIA-ALL was higher than that of CoMSIA-SEHA (0.814 and 0.785, respectively), so we choose CoMSIA-ALL model with

stronger external prediction ability as the final CoMSIA model. CoMSIA-ALL model had the highest cross-validated q^2 of 0.728 with an ONC value of 5, non-cross-validated r^2 of 0.982, the highest predictive correlation coefficient r_{pred}^2 of 0.814, a SEE value was 0.170, and an F value was 412.470. The contributions of steric, electrostatic, hydrophobic, H-donor, and acceptor field were 14.4%, 29.2%, 17.9%, 25.9% and 12.5%, respectively. The result illustrated that the electrostatic, H-bond donor and hydrophobic fields played important roles in the model. And among these three fields, the electrostatic field was the most important interaction between the ligand and the receptor protein.

Table 3 showed the results of external validation of the CoMFA-SE and CoMSIA-ALL models (hereinafter, CoMFA-SE was called CoMFA and CoMSIA-ALL was called CoMSIA). Although both CoMFA and CoMSIA models had good r_{pred}^2 values, however, according to Tropsha,⁴⁸ only high r_{pred}^2 did not show the true predictive ability of the model, only when the model satisfied condition 1, condition 2a or 2b, condition 3a or 3b, condition 4a or 4b, condition 5 and condition 6, the models had good external prediction ability. It could be seen from the Table 3 that the parameters of CoMFA and CoMSIA models satisfied all above requirements. Among them, r_m^2 was an important indicator to measure the approximation between experimental activity and predicted activity in the test set.

In addition, the results of 10 random shuffles for Y -randomization test were shown in Table 4. These results were obtained by using the dependent variable (biological activity) randomly shuffled and then using the original independent variable matrix to build new QSAR models. The q^2 and r^2 values of new QSAR models were really low. Therefore, the possibility of random correlations was ruled out. The randomly arranged bioactivities used for the test were shown in Table S1.†

The predicted activities of small molecules in the 3D-QSAR model are shown in Table 1. The plots of actual pIC_{50} against predicted pIC_{50} by the CoMFA and CoMSIA model are shown in Fig. 4, it can be seen that the black solid point and the red solid point were close to the line $Y = X$, which indicated that the actual and predicted activities of the whole data set had a strong linear relationship. The Y value of the hollow circle represented leave-one-out (LOO) cross-validated predictions.

Table 2 Statistical parameters of CoMFA and CoMSIA models based on docked pose. S – steric, E – electrostatic, H – hydrophobic, A – H-bond acceptor, D – H-bond donor

	q^2	ONC	r^2	r_{pred}^2	SEE	F value	Contributions				
							S	E	H	A	D
CoMFA-S	0.682	3	0.928	0.740	0.335	168.134	1	—	—	—	—
CoMFA-E	0.688	5	0.945	0.574	0.301	127.014	—	1	—	—	—
CoMFA-SE	0.783	4	0.944	0.851	0.3	160.128	0.394	0.606	—	—	—
CoMSIA-EHDA	0.717	6	0.989	0.812	0.135	552.841	—	0.341	0.219	0.141	0.3
CoMSIA-SHDA	0.724	3	0.958	0.811	0.257	295.325	0.242	—	0.259	0.142	0.357
CoMSIA-SEDA	0.721	4	0.972	0.791	0.213	325.942	0.201	0.365	—	0.129	0.305
CoMSIA-SEHD	0.722	3	0.942	0.807	0.302	209.989	0.179	0.356	0.197	—	0.268
CoMSIA-SEHA	0.727	2	0.977	0.785	0.194	309.365	0.182	0.417	0.244	0.156	—
CoMSIA-ALL	0.728	5	0.982	0.814	0.170	412.470	0.144	0.292	0.179	0.125	0.259



Table 3 Results of external validation parameters for CoMFA and CoMSIA

Condition	Parameters	Threshold value	CoMFA	CoMSIA
1	R^2	>0.6	0.897	0.846
2a	R_0^2	Close to value of R^2	0.896	0.831
2b	$R_0'^2$	Close to value of R^2	0.892	0.845
3a	k	$0.85 < k < 1.15$	1.046	1.029
3b	k'	$0.85 < k' < 1.15$	0.952	0.965
4a	$(R^2 - R_0^2)/R^2$	<0.1	0.001	0.018
4b	$(R^2 - R_0'^2)/R^2$	<0.1	0.005	0.001
5	$ R_0^2 - R_0'^2 $	<0.3	0.004	0.014
6	r_m^2	>0.5	0.868	0.743

Table 4 q^2 and r^2 values after several Y-randomization test

Iteration	CoMFA		CoMSIA	
	q^2	r^2	q^2	r^2
Random_1	0.001	0.152	-0.012	0.235
Random_2	-0.181	0.268	-0.225	0.445
Random_3	-0.097	0.105	-0.242	0.34
Random_4	0.237	0.345	0.219	0.373
Random_5	0.29	0.309	0.264	0.424
Random_6	0.175	0.304	0.216	0.359
Random_7	0.05	0.189	0.082	0.271
Random_8	-0.036	0.217	0.015	0.408
Random_9	0.166	0.283	0.176	0.337
Random_10	-0.031	0.134	-0.062	0.283

CoMFA contour maps

The contour maps were provided to explain the relationship between the structures and activities of compounds. The modification of small molecules according to the information given by the contour maps would be conducive to the improvement of the activity of small molecules. The contour maps were shown by StDev*Coeff type and the most active compound 54 was put into the contour maps as a reference for the explanation. The structure of compound 54 was shown in Fig. 5A.

Fig. 5B was the contour map of the CoMFA steric field. The green block means that the bulky groups were beneficial for activity, while the yellow block means the bulky groups were disfavored. Around R_3 of compound 54, there was a green contour, indicating that increasing the volume at R_3 was conducive to improve the activity. For example, compound 13 ($pIC_{50} = 5.658$) and 20 ($pIC_{50} = 5.143$) introduced medium-sized substituents in R_3 , and their activity improved compared with compound 1 ($pIC_{50} = 4.59$, $R_3 = H$). There was a green contour at N33 of compound 54, illustrating substituent R_2 length increases to R_2' appropriately, which was beneficial for the improvement of the activity. For example, the activities of compounds 26 ($pIC_{50} = 7.046$) and 36 ($pIC_{50} = 7.745$) were greater than compounds with no substituent at R_2 such as compounds 1 ($pIC_{50} = 4.59$). R_2 of compound 31 ($pIC_{50} = 5.824$) had substituent, but it did not reach the green block at N33 in

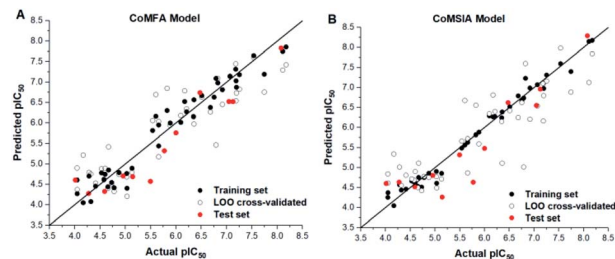


Fig. 4 Plots of experimental activities against predicted activities by the optimal of CoMFA model (A) and CoMSIA model (B). Hollow circle indicated a scatter plot of LOO cross-validated.

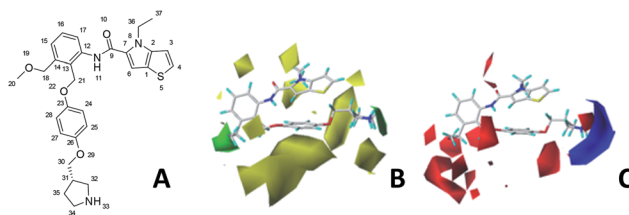


Fig. 5 (A) Structure of compound 54. CoMFA contour maps were based on compound 54 as the template. (B) Steric contour maps: green and yellow displayed the favorable and unfavorable region. (C) Electrostatic contour maps: blue and red indicated favorable and unfavorable region.

Fig. 5B, so its activity was not significantly improved. A yellow contour appeared near the R_1 , indicating that the bulky volume at R_1 was not conducive to the activity, such as the activities arrangement of 6 ($pIC_{50} = 4.274$, $R_1 = Pr$) < 5 ($pIC_{50} = 4.318$, $R_1 = CH_2CH_2NH_2$) < 4 ($pIC_{50} = 5.032$, $R_1 = Et$). Another large yellow contour appeared below hydroquinone in compound 54, indicating that increasing the volume here was not useful for the improvement of activity. Such as R_2' on *ortho* substitution of the benzene of compound 28 ($pIC_{50} = 4.166$) touched the yellow color contour, R_2' on of *meta* substitution of the benzene of compound 27 ($pIC_{50} = 6$) also contacted the yellow color contour, therefore compounds 27 and 28 reduced significantly in activity.

The contour map of the CoMFA electrostatic field was shown in Fig. 5C. The red block means that the electronegative groups were beneficial for activity, while the blue block means the electropositive groups were favorable. There were two red contours around O22 and O29 in Fig. 5C, which indicated that the addition of electronegative group can improve the activity. For example, the activity of compound 26 ($pIC_{50} = 7.046$) was higher than compound 29 ($pIC_{50} = 6.752$), because the oxygen atom was at the Y of compound 26 and the carbon atom was at the Y of compound 29. For 31 ($pIC_{50} = 5.824$) and 34 ($pIC_{50} = 5.602$) compounds, the electronegativity of R_2' substituents was weak, but they touched the O29 in red color contour, so the activities of these compounds were weaker. The presence of red contour around O19 indicated that R_3 should replace group with strong electronegativity, such as compound 7 ($pIC_{50} = 4.728$, $R_3 = Cl$) and 9 ($pIC_{50} = 4.654$, $R_3 = F$), which were more



active than compound **1** ($pIC_{50} = 4.59$, $R_3 = H$). Blue color block appeared at N33 illustrated that the increase of electropositive at R_2 was beneficial for activity. The compounds **54** ($pIC_{50} = 8.174$) and **55** ($pIC_{50} = 8.108$) with the electropositive group at R_2 were the most active in all series of compounds.

CoMSIA contour maps

Fig. 6A and B were respectively contour maps of the steric field and electrostatic field of the CoMSIA model, which conclusion were consistent with CoMFA model. For example, in the steric field, a green contour appeared at the C23 and C31 position of molecule **54**, which also expressed the need to increase the length of R_2 . Fig. 6C was the contour map of the hydrophobic field. The yellow block means that the hydrophobic groups were beneficial for activity, while the white block means the hydrophilic groups were favorable.

A large yellow block was around C23 and C26 of compound **54**, illustrating that improving the hydrophobicity of the intermediate part of R_2 would be conducive to activity. For example, in the middle part of R_2 , compound **32** ($pIC_{50} = 5.57$) was piperidine, while compound **29** ($pIC_{50} = 6.752$) was benzene. Benzene was more hydrophobic than piperidine, so the activity of compound **29** was greater than **32**. A small piece of white color in R_2 , demonstrated that adding hydrophilic group was beneficial for activity, R_2 of **50** ($pIC_{50} = 7.18$) and **51** ($pIC_{50} = 8.076$) were replaced by piperidine and pyrrolidine, respectively, so they had high activity. There was also a white contour around C14, indicating that increasing the hydrophilicity of R_3 could improve the activity. R_3 of compound **18** ($pIC_{50} = 4.599$) contained benzene, so the reason for its low activity could be explained. The R_3 of **7** ($pIC_{50} = 4.728$, $R_3 = Cl$) and **9** ($pIC_{50} = 4.654$, $R_3 = F$) were hydrophobic halogens, so their activities were not high. Contour maps of H-bond donor and acceptor are shown in Fig. 6D, the cyan contour represented that adding H-bond donor groups was beneficial for activity and the purple

contour represented that H-bond donor groups were unfavorable, the magenta color contour expressed H-bond acceptor groups had a positive effect in activity and the red color contour implied H-bond acceptor groups had a negative impact in activity. A large cyan contour appeared at N33 of compound **54**, indicating that the addition of H-bond donor group here would increase the activity. The docking results also showed that compound **54** formed a hydrogen bond with Asp555 of LSD1. R_2 of **39** ($pIC_{50} = 6.827$) had piperidine as a hydrogen bond donor, and R_2 end of **41** ($pIC_{50} = 6.346$) was ethyl, therefore the activity of **39** was higher than **41**. The magenta contour appeared around C20, indicating that the introduction of hydrogen bond acceptor group in R_3 would improve the activity, such as **16** ($pIC_{50} = 4.873$, $R_3 = CH_2OMe$) > **1** ($pIC_{50} = 4.59$, $R_3 = H$).

There was no outlier in the CoMFA model, but in the CoMSIA model, the activity of compound **32** was underestimated and became an outlier, which was also the reason why the r_{pred}^2 value of the CoMFA model was high. The structure of compound **32** was different from analog **54** (the most active compound in the series). The bulky substituent composed of two rotatable rings at R_2 in compound **32** may allow the distal ring to reach the additional area of the binding pocket, and therefore inducing different binding and modes of actions. As for the reason of inaccurate prediction, the R_2 of **32** was extended and touched the green color block in Fig. 6B from the steric field analysis, which were beneficial for the predictive value for compound **32** activity. As shown in Fig. 6C, a red color block appeared at O29, indicating that the introducing of electronegativity atoms was beneficial for activity, whereas carbon atom at the position of compound **32** had weak electronegativity, which had a negative impact on the predicted activity of compound **32**. From the hydrophobic field analysis, the larger yellow color block in Fig. 6C showed that if the hydrophobic group was located here, the activity would be improved, but the piperidine of **32** did not satisfy this condition, so it was not conducive to the predictive activity for compound **32**. In the CoMSIA model, the contribution of the steric field was 14.4%, the contribution of the electrostatic field was 29.2% and that of the hydrophobic field was 17.9%. This showed that the electrostatic field and hydrophobic field had a greater impact on activity prediction, so compound **32** was underestimated and became an outlier. There is no hydrophobic field involved in the CoMFA model, so **32** was not an outlier in the CoMFA model.

Docking analysis

We hope to explain the difference of activity between small molecules through molecular docking, to understand what binding mechanisms will benefit the interaction between ligand and protein, and to provide ideas for the future design of small molecules. Therefore, three representative compounds were chosen for docking analysis: compound **1** was the common structure of this series of compounds. Compound **28** with extended R_2 substituents was not increased but decreased in activity. The compound **54** had the highest activity.

As shown in Fig. 7A for compound **1**, the thiophene-pyrrole ring was surrounded by Val333, Thr335, Phe538, Trp695, Ala809

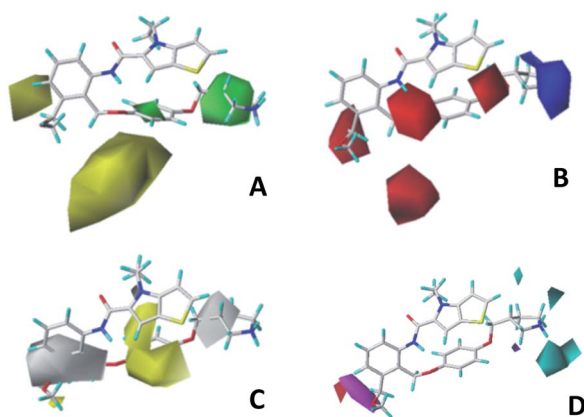


Fig. 6 CoMSIA contour maps were based on compound **54** as template. (A) Steric field: green and yellow displayed the favorable and unfavorable region. (B) Electrostatic fields: blue and red indicated favorable and unfavorable region. (C) Hydrophobic field: yellow and grey represented favorable and unfavorable region. (D) Hydrogen bond donor: cyan and purple indicated favorable and unfavorable region, and hydrogen acceptor fields: magenta and red illustrated favorable and unfavorable region.



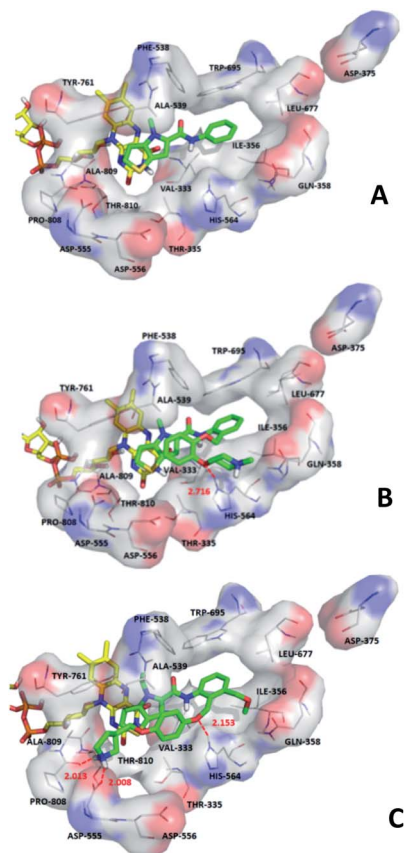


Fig. 7 Docking results of the compounds **1** (A), **28** (B), **54** (C) with LSD1, respectively. Compounds are shown in green stick model. FAD was shown in yellow stick model. The nitrogen, oxygen, sulfur atoms are shown in blue, red, yellow, respectively. Hydrogen bonds are shown in red dash lines.

and Thr810, and thiophene–pyrrole ring and FAD formed an aromatic–aromatic interaction. Benzamide was surrounded by residues of Val333, Trp695 and Phe538. The reason why the low activity of compound **1** was that there was no hydrogen bond at all. It was observed that Asp555 and Asp556 belonged to the electronegative region and was also a hydrogen-bond receptor residue. Therefore, for the series of compounds, introducing positive groups at R_2 and the formation of hydrogen bond with Asp555 and Asp556 were a potential modification method. The conclusion was also confirmed by the results of the 3D-QSAR analysis.

Compound **28** was shown in Fig. 7B, *ortho*-substitution of benzene rings in benzamide was performed, and the thiophene–pyrrole ring formed an aromatic–aromatic interaction with FAD. The substituents on the benzamide formed a hydrogen bond with His564 (His564–NH \cdots O, bond length 2.72 Å). Due to the piperidine ring replaced the *ortho*-position H of the benzene ring, the electropositive substituents did not extend to the electronegative region at Asp555, which was also the reason why the activity of compound **28** was not high enough. Meanwhile, it was verified with QSAR to explain why there were large yellow blocks under hydroquinone in the CoMFA contour maps. Compound **28** was in the cavity, but the

small molecule was still some distance away from the electronegativity region at Asp555, indicating that there was still potential for further improvement of activity.

For compound **54**, thiophene–pyrrole heterocyclines still interacted with FAD to form an aromatic–aromatic interaction. As shown in Fig. 7C, the benzene ring of benzamide was approached by *ortho*–*meta* double substitution. The *ortho*-substituents extended to the electronegative region of Asp555, where the basic N on pyrrolidine formed a hydrogen bond (Asp555–HO \cdots HN, bond length 2.01 Å) with Asp555 and another hydrogen bond with Pro808 (Pro808=O \cdots HN, bond length 2.01 Å). This result was consistent with the analysis of the electrostatic field and the hydrogen bond donor field in QSAR. Furthermore, compound **54** formed a hydrogen bond (His564–NH \cdots O, bond length 2.15 Å) with His564. In addition, the compound interacted with the Asp555 electronegative region to form a salt bridge. This analysis explained why compound **54** was the highest in activity. At the same time, we observed that Asp375 was also an electronegative region and a residue of hydrogen bond acceptor, but small molecules were still some distance away from this region. If they interact with this region, the activity of small molecules may be further enhanced, which could be used as the next direction to modify such small molecule inhibitors.

In addition, 2D diagram of compounds **1**, **28**, **54** was obtained by using open source software LigPlotPlus.⁴⁹ As shown in Fig. S4,[†] compounds **1** and **28** with poor activity had little interaction with the surrounding amino acids. Some amino acids in the binding site, Val333, Thr335, Ile356, Gln358, Phe538, Ala539, Leu659, Leu677, Trp695, Tyr761, Ala809, and Thr810 were involved in hydrophobic interactions with compound **54**. In addition, Asp555, His564, Pro808 were involved in H-bond interactions with compound **54**. Therefore, those interactions had an important impact on inhibitory activity. We found that the reason for the difference of inhibitor activity could be reasonably explained, indicating that binding mode might be the actual binding mode of small molecules. For newly designed small molecules, using molecular docking to observe the interaction between small molecules and LSD1 is very important for preliminary prediction of the activity of new small molecule inhibitors. When selecting the docking results of newly designed small molecules, we can rely on the above information for reference.

Design of novel derivatives

The structure–activity relationship (SAR) information revealed by the above 3D-QSAR contour maps analysis was summarized as shown in Fig. 8, which may be helpful in designing new LSD1 inhibitors with high activity.

R_1 substituents should not be too large, R_2 substituents should be appropriately increased in order to achieve the length of electronegativity region, and the structure of hydroquinone played an important role in improving the activity. Because this structure not only increased the volume of R_2 , but also conformed to the suggestion of improving the activity of electrostatic field. For example, it was required to add electronegative



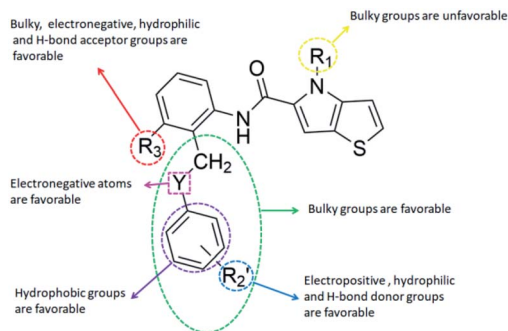
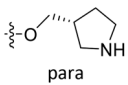
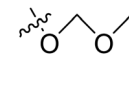
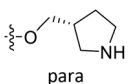
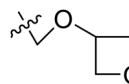
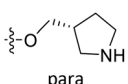
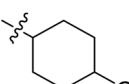
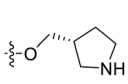
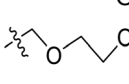
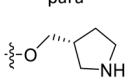
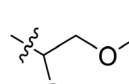
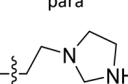
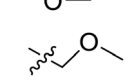
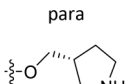
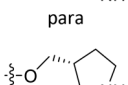
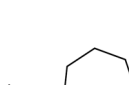


Fig. 8 Structure–activity relationship (SAR) information obtained from 3D-QSAR study.

groups at O22 and O29 positions of template compound **54**, which was also of great significance in the hydrophobic field, therefore, this structure was retained when designing new inhibitors. R_2 substituent should introduce electropositive substituent.

The addition of H-bond donor field at the R_2 showed favorable to increase activity and the introduction of hydrogen bond acceptor groups in R_3 could improve the activity. Based on scaffold in Fig. 8, we designed eight new small molecules and

Table 5 Structures and predicted activities for novel designed compounds

No.	Y	R_1	R_2	R_3	Predict pIC_{50}	
					CoMFA	CoMSIA
D1	O	Et			7.681	7.606
D2	S	Et			7.786	8.096
D3	O	Et			7.868	7.608
D4	O	Et			8.129	8.312
D5	O	Et			8.179	8.521
D6	O	Et			7.534	8.131
D7	O	CH ₃		COH	7.686	7.527
D8	O	Et			8.073	8.473

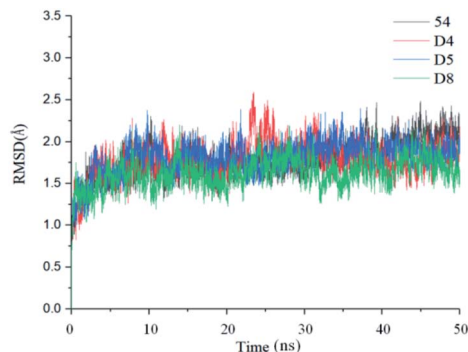


Fig. 9 RMSD values of the complexes during 50 ns MD simulations.

used 3D-QSAR model to predict their activity. The structure and prediction results of small molecules are shown in Table 5. As mentioned before, the interaction between small molecules and LSD1 was an important basis for predicting the activity of small molecules. Therefore, we selected **D4**, **D5** and **D8** with high activity for molecular docking. In the process of molecular docking, we preferentially chose binding mode with the same orientation as the binding mode obtained above and higher docking score.

MD simulations

In order to further analyze the dynamic interactions of ligand–receptor and explore the binding mode of new designed small molecules, we chose the docking results of compound **54**, **D4**, **D5**, **D8** and conducted the molecular dynamics simulation of 50 ns. The RMSD plot of $C\alpha$ for complexes was shown in Fig. 9. After a few time, the RMSD fluctuates of the four complexes were all in a very small range between 1.3 Å and 2.4 Å, which indicated that the systems had reached a state of stability. Plots of temperature and total-energy *versus* time are shown in Fig. S5 and S6.†

We compared the LSD1–**54** complex conformation between the after MD structure and initial structure, as is shown in Fig. 10, we found that compound **54** not only remained at the docking site, but also entered the active pocket of histone H3 deeper than the initial structure and blocked the entry of histone H3 into the active site, this prevented further interaction between H3 and FAD. At the same time, these results validated the reliability of the docking results.

The average MD structure was shown in Fig. 11. The thiophene–pyrrole ring was more closely connected with FAD, and small molecules formed a salt bridge with Asp555. Although compound **54** had no interaction with Pro808, it formed shorter H bonds with Asp555 (Asp555–HO \cdots HN, bond length 1.81 Å) and His564 (His564–N \cdots HN, bond length 2.55 Å). This was the reason why compound **54** had higher activity.

We superimposed the average structures of **D4**, **D5**, **D8** complexes during MD equilibrium stage to docking results, which are shown in Fig. 12. After 50 ns MD, the 3 new small molecules were still in the active pocket, the molecules formed aromatic–aromatic interaction with FAD and salt bridge with



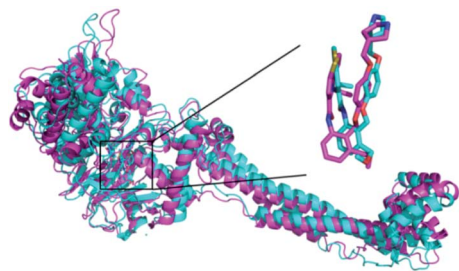


Fig. 10 Compound 54 and LSD1 of complex structure alignment between the initial structure (cyan) and MD structure (violet). The protein was shown in cartoon and ligand was shown in stick. The nitrogen, oxygen and sulfur atoms are shown in blue, red and orange, respectively.

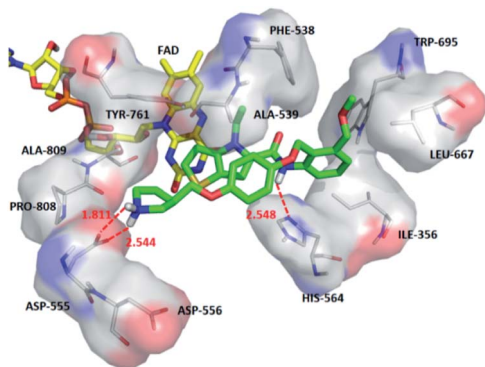


Fig. 11 The binding mode of compound 54 with LSD1 after a 50 ns MD simulation. Compound 54 and surrounding residues are shown in green stick model and white line model. Hydrogen bonds are shown in dash lines.

Asp555. The **D4** docking results showed that small molecules form hydrogen bonds with Pro808 (Pro808=O \cdots HN, bond length 2.00 Å) and Asp555 (Asp555-HO \cdots HN, bond length 1.99 Å). Although hydrogen bond lost with Pro808 during MD, shorter H-bond Asp555 (Asp555-HO \cdots HN, bond length 1.73) and new H-bond (Asn535-NH \cdots O, bond length 1.67 Å) were formed. The docking results and MD average structure showed that **D5** and Asp555 established shorter H-bond (Asp555-HO \cdots HN, bond length 1.88) during MD simulation. In addition, small molecules formed 3 new hydrogen bonds with Asn535 (Asn535-NH \cdots O, bond length 1.99), Pro808 (Pro808=O \cdots HN, bond length 1.81 Å) and His564 (His564-N \cdots HN, bond length 2.61 Å), which is attributed the predictive activity associated with **D5**.

The docking result of **D8** showed that small molecules form hydrogen bonds with Pro808 (Pro808=O \cdots HN, bond length 2.06) and Asp555 (Asp555-HO \cdots HN, bond length 2.09), respectively. At the same time, small molecules formed hydrogen bond with Asn535 (Asn535-NH \cdots O, bond length 1.89). During MD simulations, although H-bond was lost with Pro808, shorter H-bonds were formed with Asp555 (Asp555-HO \cdots HN, bond length 1.93) and Asn535 (Asn535-NH \cdots O, bond length 1.66). MD analysis indicated that **D4**, **D5**, **D8** form

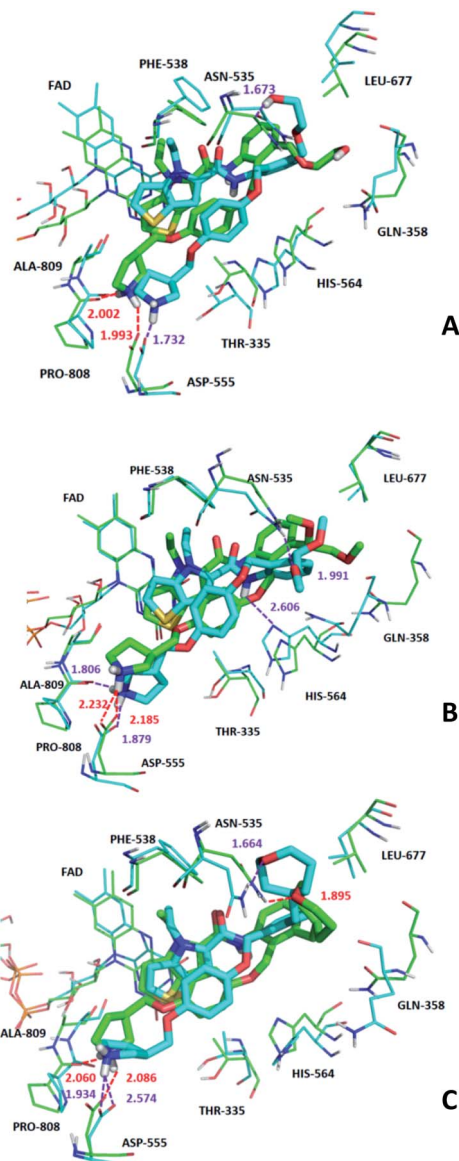


Fig. 12 The superposition of the docking structures and MD average structures of compound **D4** (A), **D5** (B), **D8** (C). Carbon atoms of docking result and MD average structure are shown in green and cyan, respectively. H-bond of docking result and 50 ns MD result are shown in red dash line and purple dash line, respectively.

favorable interaction with LSD1. In the meantime, the importance of Asp555 for the activity of these small molecules was proved. In accordance with the previous QSAR model and docking analysis, R_3 was modified according to the QSAR contour map (enlarging volume and adding hydrogen bond acceptor groups). After these modifications, we found that the R_3 groups of **D4**, **D5** and **D8** compounds formed hydrogen bonds with Asn535 in the superposition, among these excellent compounds reported, none of them formed H-bond with Asn535, which may be the reason why **D4**, **D5** and **D8** have higher predictive activity than compound 54. The modification of R_3 and Asn535 deserve the attention of future designers of such inhibitors.



Table 6 Binding free energies of ligand–protein complex

No.	ΔE_{ele} kcal mol ⁻¹	ΔE_{vdw} kcal mol ⁻¹	ΔG_{GB} kcal mol ⁻¹	ΔG_{SA} kcal mol ⁻¹	ΔG_{sol} kcal mol ⁻¹	ΔG_{bind} kcal mol ⁻¹	pIC ₅₀ predicted
LSD1-54	-103.7501	-52.4748	128.9897	-6.6194	122.3703	-33.8537	8.174
LSD1-D4	-134.9198	-49.4678	151.9764	-6.5057	145.4707	-38.9169	8.312
LSD1-D5	-101.5999	-61.0727	120.0679	-7.7538	112.3141	-50.3592	8.521
LSD1-D8	-86.1198	-59.8317	109.082	-7.9847	101.0974	-44.8516	8.473

In addition, it was found that small molecules and FAD formed aromatic–aromatic interaction before and after MD, which was of great significance to the binding mode of these small molecules.

Binding free energy calculation

In order to further verify the binding affinity of **D4**, **D5**, **D8** with LSD1, the binding free energies of the three compounds with LSD1 were calculated by MM/GBSA method, and the binding free energy of compound **54** with LSD1 was also computed as a reference. The results are shown in Table 6.

The binding free energies of compounds **54**, **D4**, **D5**, **D8** with LSD1 were -33.85 kcal mol⁻¹, -38.92 kcal mol⁻¹, -50.36 kcal mol⁻¹, -44.85 kcal mol⁻¹, respectively. It is generally believed that the lower of ΔG_{bind} value, the more stable of the complex. Table 6 showed that ΔG_{bind} values were coincided well with the predicted pIC₅₀ values of the QSAR model. The electrostatic energy ΔE_{ele} contributed much more to the binding free energy than other energies, indicating that electrostatic interaction played a key role in the complex system, which could be caused by the interaction between basic N in small molecules and Asp555 negative region. Similarly, the van der Waals energy ΔE_{vdw} illustrated that hydrophobic interaction was also important in the binding process. The polar solvation energy ΔG_{GB} is positive, indicating that it was not conducive to ΔG_{bind} , the reason was that excessive binding pocket could cause exposure of ligand to solvents. However, ΔG_{SA} values were negative, which means that non-polar solvation energy was beneficial for ΔG_{bind} . Because the newly designed compounds **D4**, **D5** and **D8** had lower ΔG_{bind} values than **54**, they may have a stronger inhibitory effect on LSD1.

In order to analyze which amino acids contributed more to the binding free energy of the system, we decomposed the

binding free energy into each amino acid and observed that the amino acids that contribute more to the binding free energy were Val333, Asn535, Phe538, Asp555, Leu677, Trp695, Tyr761 and FAD. Their energy contributions are shown in Fig. 13. It was found that Asp555 contributed the most to the four systems, which again showed that Asp555 was closely related to the activities of these small molecules. Furthermore, FAD contributed a lot to the four systems. The docking results showed that thiophene–pyrrole and FAD had aromatic–aromatic interaction, which was important for the binding mode of these small molecules. **D4**, **D5** and **D8** formed hydrogen bond with Asn535 and compound **54** did not form hydrogen bond with it, therefore Asn535 was beneficial for the binding free energy of **D4**, **D5**, **D8**, but has little contribution to the binding with compound **54**. Although Asp555 contributed less to **D5** than **D4**, Asn535, Phe538 and TRP695 contributed more to **D5** than **D4**, which may be the reason why **D5** activity was higher than **D4**.

ADME and bioavailability analysis

It is necessary to carry out bioavailability and pharmacokinetics prediction on the novel candidate compounds before the experiment. We predicted the candidate compounds **D4**, **D5** and **D8**, and compound **54** with the best activity was selected as the control group. The results are shown in Table 7.

Compound saturation was measured by fraction Csp³ and polarity was calculated by TPSA (topological polar surface area). Lipophilicity used log *P* to quantify. The log *P* values of **D4**, **D5** and **D8** were in the best range, which indicated that they had good absorbency. log *S* was used to measure solubility, and the log *S* values of **D4**, **D5** and **D8** were also within a reasonable range, which demonstrated that they had good solubility. The only indicator for **D4**, **D5** and **D8** beyond the best range was num. rotatable bonds, which mean that the molecules had high flexibility in the human body. So we need to minimize the number of rotational bonds in the design of such small molecules in the future. Overall, **D4**, **D5** and **D8** had really high bioavailability. High stands for compounds **54**, **D4** and **D5** with good gastrointestinal absorption ability. Low means that **D8** may not have gastrointestinal absorption ability. No represented that compounds **54**, **D4**, **D5** and **D8** were not brain penetrant. The two properties could be more intuitively reflected from Fig. S7.† Yes represented that these compounds had inhibitory effects on CYP3A4 and could be excreted through metabolic biotransformation. Skin permeability was measured by log *K_p*, and **D8** had highest skin permeability. Finally, Lipinski's rule was used to evaluate the drug-likeness of four compounds. The results were yes. The bioavailability and ADME

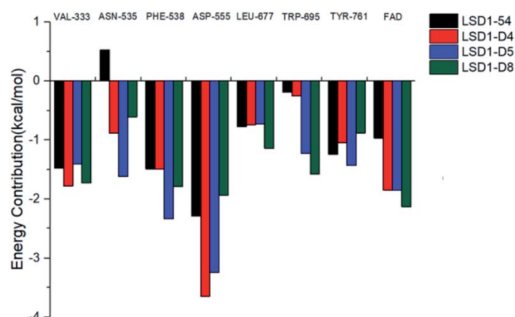


Fig. 13 Binding free energy decomposition plots.



Table 7 Bioavailability and pharmacokinetics prediction. *N*-number of rotatable bonds

No.	MW (g mol ⁻¹)	Fraction Csp ³	<i>N</i>	TPSA (Å ²)	log <i>P</i>	log <i>S</i>	HIA	BBB	CYP3A4 inhibition	log <i>K_p</i> (cm s ⁻¹)	Drug-likeness Lipinski
54	519.66	0.34	12	101.99	4.44	-5.37	High	No	Yes	-6.43	Yes
D4	549.68	0.37	14	122.22	4.12	-4.97	High	No	Yes	-7.10	Yes
D5	563.71	0.39	14	111.22	4.56	-5.41	High	No	Yes	-6.78	Yes
D8	587.77	0.44	12	101.99	4.90	-6.73	Low	No	Yes	-5.73	Yes
Optimal range	<800	0.25–1	≤10	20–130	-0.7 to 5	-10 to 6	—	—	—	—	—

analysis showed that the novel designed compounds might become safer and more active LSD1 inhibitors.

Conclusions

In this study, we chose the series of thieno[3,2-*b*]pyrrole-5-carboxamides as reversible LSD1 inhibitors using molecular docking, 3D-QSAR. ECIDALs was followed when selecting docking results.³³ The representative results of molecular docking for small molecules were used to explain the differences in biological activity. The CoMFA ($q^2 = 0.783$, $r^2 = 0.944$) and CoMISA models ($q^2 = 0.728$, $r^2 = 0.982$) were received to perform molecular modeling study. The results showed that the models had good internal verification ability and external prediction ability. The models were further validated following the criteria given by Tropsha and Roy, and were determined to be statistically reliable and robust. We could use this model to predict the activity of this series of compounds to reduce the loss of blind investment in the experiment. Likewise, the contour maps also indicated the relationship between the structure and activity of small molecules. The results of molecular docking and the information prompted by contour maps confirmed each other. Based on these 3D-QSAR models, 8 new small molecules were designed *in silico*. Further docking, MD, calculation of binding free energy, ADME and bioavailability prediction were carried out for these designed compounds and the results indicated that D4, D5 and D8 show good potential to become LSD1 inhibitors with better activity than compound 54. At the same time, key amino acids affecting the activity of these inhibitors, such as Asp555, Pro808, His564, were easy to form H-bonds with small molecules, after R₃ was modified, Asn535 formed H-bond with small molecules. Val333, Phe538, Leu677, Trp695, Thr761 and FAD could enable inhibitors to maintain stability in the binding site. Our study would provide some theoretical guidance for the future design novel reversible LSD1 inhibitor.

Conflicts of interest

There are no conflicts to declare.

Acknowledgements

The authors are grateful for the financial support from The National Natural Science Foundation of China (Grant No. 21603180), The Research Project of Henan Provincial

Department of Science and Technology (Grant No. 182102210122) Research Project of Xinxiang Medical University (Grant No. 505060, 505144, 505212) and Open Topic at School of Biomedical Engineering, Xinxiang Medical University (Grant No. 2018-BME-KFKT-01, 2018-BME-KFKT-10, 2018-BME-KFKT-11). The authors also thank Prof. Zheng Jie from the Guangdong University of Technology for offering software support and Dr Meilan Huang from Queens University Belfast helpful discussion.

References

- 1 B. D. Strahl and C. D. Allis, *Nature*, 2000, **403**, 41–45.
- 2 T. Kouzarides, *Cell*, 2007, **128**, 693–705.
- 3 Y. Shi, F. Lan, C. Matson, P. Mulligan, J. R. Whetstone, P. A. Cole, R. A. Casero and Y. Shi, *Cell*, 2004, **119**, 941–953.
- 4 B. Laurent, L. Ruitu, J. Murn, K. Hempel, R. Ferrao, Y. Xiang, S. Liu, B. A. Garcia, H. Wu and F. Wu, *Mol. Cell*, 2015, **57**, 957–970.
- 5 I. Garciasbassets, Y. Kwon, F. Telese, G. G. Prefontaine, K. R. Hutt, C. S. Cheng, B. Ju, K. A. Ohgi, J. Wang and L. Escoubetlozach, *Cell*, 2007, **128**, 505–518.
- 6 J. Huang, R. Sengupta, A. Espejo, M. G. Lee, J. Dorsey, M. Richter, S. Opravil, R. Shiekhattar, M. T. Bedford and T. Jenuwein, *Nature*, 2007, **449**, 105–108.
- 7 J. Wang, S. Hevi, J. K. Kurash, H. Lei, J. Bajko, H. Su, W. Sun, H. Chang, G. Xu and F. Gaudet, *Nat. Genet.*, 2009, **41**, 125–129.
- 8 E. Nunez, Y. Kwon, K. R. Hutt, Q. Hu, M. D. Cardamone, K. A. Ohgi, I. Garciasbassets, D. W. Rose, C. K. Glass and M. G. Rosenfeld, *Cell*, 2008, **132**, 996–1010.
- 9 Y. J. Shi, C. Matson, F. Lan, S. Iwase, T. Baba and Y. Shi, *Mol. Cell*, 2005, **19**, 857–864.
- 10 A. A. Lokken and N. J. Zeleznikle, *Cancer Cell*, 2012, **21**, 451–453.
- 11 T. Lv, D. Yuan, X. Miao, Y. Lv, P. Zhan, X. Shen and Y. Song, *PLoS One*, 2012, **7**, e35065.
- 12 C. Magerl, J. Ellinger, T. Braunschweig, E. Kremmer, L. K. Koch, T. Holler, R. Buttner, B. Luscher and I. Gutgemann, *Hum. Pathol.*, 2010, **41**, 181–189.
- 13 J. H. Schulte, S. Lim, A. Schramm, N. Friedrichs, J. Koster, R. Versteeg, I. Ora, K. W. Pajtler, L. Kleinhitpass and S. Kuhfittigkulle, *Cancer Res.*, 2009, **69**, 2065–2071.
- 14 Y. Wang, H. Zhang, Y. Chen, Y. Sun, F. Yang, W. Yu, J. Liang, L. Sun, X. Yang and L. Shi, *Cell*, 2009, **138**, 660–672.



- 15 Y. C. Zheng, B. Yu, G. Z. Jiang, X. J. Feng, P. X. He, X. Y. Chu, W. Zhao and H. M. Liu, *Curr. Top. Med. Chem.*, 2016, **16**, 2179–2188.
- 16 T. E. Mcallister, K. S. England, R. J. Hopkinson, P. E. Brennan, A. Kawamura and C. J. Schofield, *J. Med. Chem.*, 2016, **59**, 1308–1329.
- 17 Y. Zheng, B. Yu, Z. Chen, Y. Liu and H. Liu, *Epigenomics*, 2016, **8**, 651–666.
- 18 D. M. Z. Schmidt and D. G. Mccafferty, *Biochemistry*, 2007, **46**, 4408–4416.
- 19 M. G. Lee, C. Wynder, D. M. Z. Schmidt, D. G. Mccafferty and R. Shiekhatar, *Chem. Biol.*, 2006, **13**, 563–567.
- 20 T. Maes, C. Mascaro, I. Tirapu, A. Estiarte, F. Ciceri, S. Lunardi, N. Guibourt, A. Perdones, M. M. Lufino and T. C. P. Somerville, *Cancer Cell*, 2018, **33**, 495.
- 21 C. A. Stewart and L. A. Byers, *Cancer Cell*, 2015, **28**, 4–6.
- 22 F. Wu, C. Zhou, Y. Yao, L. Wei, Z. Feng, L. Deng and Y. Song, *J. Med. Chem.*, 2016, **59**, 253–263.
- 23 V. Sorna, E. R. Theisen, B. Stephens, S. L. Warner, D. J. Bearss, H. Vankayalapati and S. Sharma, *J. Med. Chem.*, 2013, **56**, 9496–9508.
- 24 L. Sartori, C. Mercurio, F. Amigoni, A. Cappa, G. Faga, R. Fattori, E. Legnaghi, G. Ciossani, A. Mattevi and G. Meroni, *J. Med. Chem.*, 2017, **60**, 1673–1692.
- 25 P. Vianello, L. Sartori, F. Amigoni, A. Cappa, G. Faga, R. Fattori, E. Legnaghi, G. Ciossani, A. Mattevi and G. Meroni, *J. Med. Chem.*, 2017, **60**, 1693–1715.
- 26 W. L. Jorgensen, *Science*, 2004, **303**, 1813–1818.
- 27 P. P. Qian, S. Wang, K. R. Feng and Y. J. Ren, *RSC Adv.*, 2018, **8**, 14311–14327.
- 28 Y. Fang, Y. Lu, X. Zang, T. Wu, X. Qi, S. Pan and X. Xu, *Sci. Rep.*, 2016, **6**, 23634.
- 29 S. Ma, S. Zhou, W. Lin, R. Zhang, W. Wu and K. Zheng, *RSC Adv.*, 2016, **6**, 100772–100782.
- 30 R. D. Cramer, D. E. Patterson and J. D. Bunce, *J. Am. Chem. Soc.*, 1988, **110**, 5959–5967.
- 31 G. Klebe, U. Abraham and T. Mietzner, *J. Med. Chem.*, 1994, **37**, 4130–4146.
- 32 C. Munozgutierrez, F. Adasmecarreno, E. Fuentes, I. Palomo and J. Caballero, *RSC Adv.*, 2016, **6**, 64756–64768.
- 33 J. Chen, R. Yu, B. Shen, Y. Xu, Y. Liu, H. Zheng and W. Yao, *Med. Chem. Res.*, 2013, **22**, 1730–1739.
- 34 H. Duan, X. Liu, W. Zhuo, J. Meng, J. Gu, X. Sun, K. Zuo, Q. Luo, Y. Luo and D. Tang, *Mol. Simul.*, 2019, **45**, 694–705.
- 35 G. Klebe and U. Abraham, *J. Comput.-Aided Mol. Des.*, 1999, **13**, 1–10.
- 36 P. K. Balasubramanian, A. Balupuri, C. G. Gadhe and S. J. Cho, *Med. Chem. Res.*, 2015, **24**, 2347–2365.
- 37 R. D. Clark and P. C. Fox, *J. Comput.-Aided Mol. Des.*, 2004, **18**, 563–576.
- 38 L. Ding, Z. Wang, X. Sun, J. Yang, C. Ma, W. Li and H. Liu, *Bioorg. Med. Chem. Lett.*, 2017, **27**, 3521–3528.
- 39 V. Srivastava, S. P. Gupta, M. I. Siddiqi and B. N. Mishra, *Eur. J. Med. Chem.*, 2010, **45**, 1560–1571.
- 40 J. Verma, V. M. Khedkar and E. C. Coutinho, *Curr. Top. Med. Chem.*, 2010, **10**, 95–115.
- 41 K. Roy, P. Chakraborty, I. Mitra, P. K. Ojha, S. Kar and R. N. Das, *J. Comput. Chem.*, 2013, **34**, 1071–1082.
- 42 M. Lorca, C. Moralesverdejo, D. Vasquezvelasquez, J. Andradeslagos, J. Campaninisinallas, J. Sotodelgado, G. Recabarrengajardo and J. Mella, *Molecules*, 2018, **23**, 1191.
- 43 C. Rucker, G. Rucker and M. Meringer, *J. Chem. Inf. Model.*, 2007, **47**, 2345–2357.
- 44 H. Sun, Y. Li, M. Shen, S. Tian, L. Xu, P. Pan, Y. Guan and T. Hou, *Phys. Chem. Chem. Phys.*, 2014, **16**, 22035–22045.
- 45 A. Daina, O. Michielin and V. Zoete, *Sci. Rep.*, 2017, **7**, 42717.
- 46 C. A. Lipinski, F. Lombardo, B. W. Dominy and P. J. Feeney, *Adv. Drug Delivery Rev.*, 1997, **23**, 3–25.
- 47 J. Caballero, M. Fernandez, M. Saavedra and F. D. Gonzaleznilo, *Bioorg. Med. Chem.*, 2008, **16**, 810–821.
- 48 A. Tropsha, *Mol. Inf.*, 2010, **29**, 476–488.
- 49 R. A. Laskowski and M. B. Swindells, *J. Chem. Inf. Model.*, 2011, **51**, 2778–2786.

